The nucleus measures shape changes for cellular proprioception to control dynamic cell behavior

Authors: Valeria Venturini[1,2], Fabio Pezzano[2], Frederic Català Castro[1], Hanna-Maria Häkkinen[2], Senda Jiménez-Delgado[2], Mariona Colomer-Rosell[1], Monica Marro[1], Queralt Tolosa-Ramon[2], Sonia Paz-López[3], Miguel A. Valverde[3], Julian Weghuber[4], Pablo Loza-Alvarez[1], Michael Krieg[1], Stefan Wieser[1,*], Verena Ruprecht[2,5,*]

[1] ICFO – Institut de Ciencies Fotoniques, The Barcelona Institute of Science and Technology, 08860 Castelldefels, Spain
[2] Centre for Genomic Regulation (CRG), The Barcelona Institute of Science and Technology, 08003 Barcelona, Spain
[3] Laboratory of Molecular Physiology, Department of Experimental and Health Sciences, Universitat Pompeu Fabra (UPF) Barcelona, Spain
[4] University of Applied Sciences Upper Austria, Stelzhamerstraße 23, Wels 4600, Austria
[5] Universitat Pompeu Fabra (UPF), Barcelona, Spain

* Correspondence to stefan.wieser@icfo.eu and verena.ruprecht@crg.eu

Abstract: The physical microenvironment regulates cell behavior during tissue development and homeostasis. How single cells decode information about their geometrical shape under mechanical stress and physical space constraints within tissues remains largely unknown. Here we show that the nucleus, the biggest cellular organelle, functions as an elastic deformation gauge that enables cells to measure cell shape deformations. Inner nuclear membrane unfolding upon nucleus stretching provides physical information on cellular shape changes and adaptively activates a calcium-dependent mechano-transduction pathway, controlling actomyosin contractility and migration plasticity. Our data support that the nucleus establishes a functional module for cellular proprioception that enables cells to sense shape variations for adapting cellular behavior to their microenvironment.

One Sentence Summary: The nucleus functions as an active deformation sensor that enables cells to adapt their behavior to the tissue microenvironment.

Main Text:

Introduction

The 3D shape of an organism is built by active force-generating processes at the cellular level and the spatio-temporal coordination of morphodynamic cell behavior. Contractility of the actomyosin cell cortex represents a major cellular force production mechanism underlying cellular shape change (*1*), cell polarization (*2*) and active cell migration dynamics (*3*). Contractility levels are regulated by the activity of non-muscle myosin II motor proteins (*4*) and are precisely controlled to tune single cell and tissue morphodynamics during development (*5, 6*) and tissue homeostasis

and disease in the adult organism (*7, 8*). Still, mechanisms that regulate the set point level of cortical contractility on the single cell level remain poorly understood.

To adjust cortical contractility levels, cells need to make quantitative measures of their mechano-chemical 3D tissue microenvironment and translate this information into a defined morphodynamic output response. During embryogenesis, morphogens that act as chemical information carriers have attracted major attention (*9*), modulating cytoskeletal and cellular dynamics via receptor signaling pathways that tune protein activities (such as phosphorylation states) and/or protein expression levels. In contrast, physical parameters of the 3D tissue niche and mechanical forces gain importance as regulators of cellular morphodynamics and myosin II-dependent cortical contractility levels (*10, 11*). In vivo, mechanical cell deformation and cellular packing density in crowded tissue regions has been shown to influence major morphodynamic processes such as cortical actomyosin contractility (*12, 13*), cell division (*14-17*), cell extrusion and invasion (*18*). Ex vivo studies further provided evidence on the single-cell level that physical cell deformation is sufficient to modulate cortical myosin II localization and motor protein activity (*19, 20*) and influence morphodynamic cell behavior (*21, 22*).

A recent example has been the identification of a fast amoeboid migration mode, termed stable-bleb migration, that is triggered by an increase in cortical contractility via genetic or physical cell perturbation(*23*). This morphodynamic migration switch was shown to be present in both undifferentiated and lineage committed embryonic progenitor cells and was further identified in various other cell types (*24-29*). This suggests that a conserved, yet unknown, mechanosensitive cellular signaling module regulates myosin II-based cortical contractility and motile cell transformation depending on cellular shape deformations in constrained tissue microenvironments.

Cell contractility levels increase upon cell confinement and regulate migration plasticity

To approach the question of how cells can measure and adaptively respond to physical cell shape changes within their 3D tissue microenvironments, we established a synthetic approach that enables to mimic mechanical cell deformations in controlled 3D microconfinement assays (*30*). Primary progenitor stem cells were isolated from blastula stage zebrafish embryos and cultured in planar confinement assays of defined height to mimic various cell deformation amplitudes (Fig. S1A). Lowering confinement height in discrete steps increased cell deformation, which scaled non-linearly with a pronounced enrichment of myosin II at the cell cortex relative to cortical actin accumulation (Fig. 1A,B and Fig. S1B-D; Movie 1). Cortical accumulation of myosin II was accompanied by an increase in cellular bleb size (Fig. S1E, Movie 1), indicative of an active increase in cortical contractility levels depending on confinement height. Myosin II re-localization to the cell cortex in confined cells was rapid ($t_{1/2} < 1$min, Fig. 1C,D) and temporally stable under confinement. Of note, distinct plateaus of cortical myosin II enrichment were evident, with myosin II re-localization increasing for larger cell deformations (Fig. 1C). A cell confinement height below 7 µm caused a pronounced increase in cell lysis during compression, defining a maximal threshold deformation of ~30% of the initial cell diameter, given a blastula cell size of d~25 µm (Fig. S3H). Overall, these data support that the physical microenvironment defines a specific set point level of cortical contractility as a function of cell deformation.

We have previously shown that an increase in myosin II-mediated cortical contractility induced a stochastic motility switch into a highly motile amoeboid migration phenotype termed stable-bleb mode (*23*). In accordance with these results, rapid cortical myosin II enrichment in confinement

resulted in spontaneous cell polarization which initiated amoeboid cell migration (Fig. 1E,F and Fig. S1F,G, Movie 2,3). Polarized cells revealed characteristic actomyosin density gradients from the cell front towards the rear accompanied with fast retrograde cortical flows (Fig. S1H, Movie 2, 3). These cortical flows have been shown to power fast amoeboid migration in polarized cells (*23, 31*), while unpolarized cells showed random tumbling with minimal net translocation (Fig. S1F,G, S2A). These data support that physical cell deformation in confinement is sufficient to increase actomyosin network contractility and trigger rapid amoeboid cell migration.

Release of cell compression induced a rapid re-localization of cortical myosin to the cytoplasm (Fig. 1G and S1I), followed by a rapid loss of cell polarization and related migratory capacity (Fig. S1G, Movie 4). Interfering with myosin II activity via Blebbistatin inhibited cell polarization and associated cell motility in confinement (Fig. 1E and S1J), in accordance with a necessary role of myosin II-based contractility in cell polarization and migration induced by mechanical cell shape deformation. Cortical myosin II enrichment and cell polarization occurred independently of caspase activation (Fig. S1K), supporting that morphodynamic changes are not caused by the activation of pro-apoptotic signaling programs. Furthermore, transcriptional inhibition did not block cortical myosin II re-localization and cell polarization (Fig. S1L), indicating that a non-genetic program is regulating cellular morphodynamics under cell compression.

During gastrulation, blastoderm embryonic progenitor stem cells specify into different lineages (ectoderm, mesoderm, endoderm) and acquire distinct biomechanical and morphodynamic characteristics, driving germ layer positioning and shape formation of the embryo (*32, 33*) (Fig. 2A,B). To test the mechanosensitive response to cell deformation at later developmental stages, we obtained different progenitor cell types from embryos via genetic induction or using endogenous reporter lines. Under confinement, non-motile ectodermal cells rapidly polarized and started to migrate in an amoeboid stable-bleb mode. Similarly, mesendodermal cells underwent a fast mesenchymal-to-amoeboid transition in confinement (Fig. 2B-D and Fig. S2A, Movie 3,5). The fraction of polarized stable-bleb cells and their cell speed was comparable for different progenitor cell types in confinement (Fig. S2B,C). Together, these results support that physical cell shape deformation in confined tissue microenvironments activates a mechanosensitive signaling pathway regulating adaptive cortical contractility levels and morphodynamic migration plasticity in pluripotent and lineage committed embryonic stem cells.

The cell nucleus is an analog mechanosensor of large cell shape deformation

We next sought to identify potential mechanisms that control cellular shape deformation sensing and adaptive morphodynamic behavior. Cortical myosin II re-localization and amoeboid cell transformation occurred on passivated confinement surfaces independently of adhesive substrate coating (Fig. S2A,C and S3A) and cell-cell contact formation (Fig. S3B). These observations support that the activation of cortical contractility in confinement occurs independently of adhesion-dependent mechano-transduction pathways (*34*). The temporal characteristics of myosin II re-localization dynamics in confined cells showing a fast, stable and reversible accumulation of cortical myosin II (Fig. 1C,D), suggested that shape deformation is sensed by a non-dissipative cellular element that can rapidly measure and convert gradual cellular shape changes into stable contractility response levels.

The actomyosin cytoskeleton itself has been implicated to act as a mechanosensitive network (*20*), but generally limits deformation sensing due to rapid turnover of the cell cortex (*35*). To test for

the activation of mechanosensitive ion channels we used Gadolinium and GsMTx4, inhibitors of stretch activated channels, with GsMTx4 having been shown to block the tension dependent Piezo1 channel which is activated following confinement of human cancer cells (*36*). Treatment with both inhibitors showed no significant reduction in cortical myosin II accumulation under cell deformation (Fig. S3C), despite the presence of functional Piezo1 channels in these cells as validated with the Piezo1 specific agonist Yoda (Fig. S3D).

Interestingly, we observed that cortical myosin II enrichment only started to occur below a threshold confinement height (~13 µm) that correlated with the spatial dimension of the nucleus (Fig. 3A and S3H). Analyzing nuclear shape change versus cortical myosin accumulation revealed a bi-phasic behavior, with a first phase in which the nucleus diameter remained nearly constant and no myosin II accumulation was observed, and a second phase in which the relative myosin accumulation linearly increased with the relative change in nucleus diameter (Fig. 3A,B and S3E). In accordance with this observation, we expected a proportional change of nuclear surface ruffling upon deformation of an initially spherical nucleus. Measuring of nuclear surface folding by the expression of the inner nuclear membrane (INM) protein Lap2b-eGFP revealed that membrane ruffling was continuously reduced when nucleus deformation started to occur at a threshold deformation of ~13 µm (Fig. 3C-E and S3F, Movie 6). In addition, analysis of nucleus membrane curvature for confined versus control cells in suspension indicated INM surface unfolding (Fig. 3F,G, Movie 6), with no significant difference in total nuclear volume and surface (Fig. S3G). Nucleus deformation further correlated with cortical myosin II accumulation in the endogenous in vivo context during the blastula to gastrula transition, when a gradient of cellular packing density appears from the animal pole towards the lateral margin (*37*) (Fig. S2D,E).

To further probe the dependence of cortical myosin II accumulation on nucleus size, we dissociated primary embryonic stem cells from early and late blastula stages as cells reduce their size in consecutive rounds of early cleavage divisions (Fig. S3H). Deforming cells of different sizes under similar confinement heights revealed that myosin II accumulation is correlated with relative changes in nucleus deformation but not cell deformation (Fig. 4A,B). To test a functional role of the nucleus in regulating cortical contractility levels during cellular shape deformation, we analyzed cortical myosin II accumulation in mitotic cells that present a disassembled nuclear envelope. To arrest cells in mitosis and further increase the percentage of mitotic cells, we used Nocodazole, a microtubule disrupting drug. Confinement of mitotic cells (either spontaneous or Nocodazole-induced) did not trigger a cortical myosin II accumulation at 7 µm confinement height compared to interphase blastula cells (Fig. 4C) or cell polarization (Fig. S3I), although they accumulated myosin II (Fig. 4D) and polarized (Fig. S3I) in response to LPA, a potent activator of Rho/Rock signaling that has previously been shown to induce rapid cortical myosin II enrichment and amoeboid migration in zebrafish embryonic progenitor stem cells (*23*). During entry into mitosis, cells further gradually lost cortical myosin II accumulations which temporally correlated with the start of nuclear envelop breakdown (Fig. 4E). Altogether, these data show that myosin II enrichment is associated with nuclear shape deformation and stable INM membrane unfolding. This suggests that the nucleus functions as a continuous non-dissipative sensor element of cell deformation involved in the mechanosensitive regulation of cortical contractility levels and cellular morphodynamics.

To directly test biophysical characteristics of the nucleus, we developed an assay to probe intracellular nucleus mechanics by optical tweezer measurements. For this purpose, latex beads of 1 µm size were injected into 1-cell stage embryos that dispersed across embryonic cells during

early cleavage cycles and acted as intracellular force probes to measure rheological properties of the nucleus (Fig. S4A). Trapezoidal loads were measured for cells in suspension and under 10 µm confinement (Fig. S4B-E). The recorded force followed the fast-initial indentation to reach a peak force before it relaxed to a non-zero constant force-plateau. The relaxation time remained unchanged between suspension (τ=6.08s +/- 1.1s) and confined cells (τ =4.00s +/- 0.6s) (Fig. S4D-H), suggesting a passive but rapid (second scale) relaxation of a viscous component. The force-plateau on long timescale corresponds to an elastic component of the nucleus (Fig. S4I), in line with previous measurements that identified an elastic behavior of the nucleus (*38*) that can act as a cellular strain-gauge. In addition, we observed that INM unfolding was stable over a measurement period of 60 min (Fig. S4J) under mechanical cell deformation, supporting that INM stretch does not relax over extended time periods.

Nuclear deformation activates a calcium-dependent mechanotransduction pathway regulating myosin II activity

We next aimed at identifying nucleus deformation-dependent signaling pathways that link the spatio-temporal correlation of nuclear shape changes with fast myosin II activation and changes in morphodynamic cell behavior. Our previous observations suggested that nucleus deformation and associated mechanosensitive processes at the INM interface are involved in the regulation of myosin II activity and cortical contractility. Among a set of molecules tested under confinement conditions (Table S1), we identified cytosolic phospholipase A2 ($cPLA_2$) as a key molecular target mediating the activation of cortical myosin II enrichment (Fig. 5A-B) and amoeboid cell transformation under cell compression (Fig. 5C). Inhibition of $cPLA_2$ by pharmacological interference using Pyrrophenone robustly blocked cortical myosin II re-localization under varying confinement heights (Fig. S5A). Furthermore, we observed a significant reduction of cortical myosin II levels in confined cells by morpholino (MO) interference with $cPLA_2$, while overexpression of $cPLA_2$ mRNA rescued the morphant phenotype and led to a comparable myosin II accumulation as in control cells (Fig. 5A,B). Residual myosin II activation in cells obtained from morphant embryos suggests a maternal contribution of cPLA2 protein in the early embryo which cannot be targeted by MO interference. To exclude that other mechanisms such as structural changes in the actin network prevent cortical myosin II re-localization under $cPLA_2$ inhibition, we added LPA as an exogenous myosin II activator to $cPLA_2$ inhibited cells. Under this condition, myosin II was strongly accumulated at the cell cortex (Fig. S5B,C) and induced cell polarization associated with amoeboid motility (Fig. 5C). These data support that myosin II can be activated by extrinsic pathways when $cPLA_2$ signaling is inhibited and remains competent to bind to the cell cortex.

Recent work identified that the activation of pro-inflammatory signaling during leucocyte recruitment to wounding sites is regulated by tension-sensitive binding of $cPLA_2$ to the INM (*39*). We thus tested a role of $cPLA_2$ in the nucleus by generating a modified $cPLA_2$ construct containing a nuclear export sequence (NES). Using Leptomycin B as a blocker of nuclear export, an accumulation of $cPLA_2$-NES-GFP within the nucleus was observed, showing a concomitant increase of cortical myosin II levels in confined cells (Fig. 6A,B). These data support, that cPLA2 localization in the nucleus is required for myosin II enrichment at the cortex.

We further validated that cortical myosin II enrichment in cells of different sizes (early versus late blastula cells) and different embryonic cell lineages (mesendoderm/ectoderm cells) depends on the

activation of cPLA$_2$ signaling. Pharmacological inhibition of cPLA$_2$ activity blocked cortical myosin re-localization in confined cells (Fig. 6C) and strongly reduced cell polarization and associated migration competence (Fig. S2B), supporting a consistent role of cPLA$_2$ activation under physical cell deformation across early to late developmental stages. These data support that activation of cPLA$_2$ signaling in the nucleus mediates adaptive cytoskeletal and morphodynamic behavior under cell deformation.

Arachidonic acid (AA) is the primary cleavage product generated by cPLA$_2$ activity (*40*). To directly validate whether nucleus deformation in confinement triggers cPLA$_2$ activity, we measured the release of AA by Raman spectroscopy. The analysis of Raman spectra confirmed the specific production of AA in confined cells (Fig. 6D and Fig. S5E), with the increase in AA production in confined versus control cells being specifically blocked in the presence of cPLA$_2$ inhibitor (Fig. 6E). We further observed that AA was exclusively detected in the cytoplasm of confined cells, arguing that AA is directly released from nuclear membranes into the cytoplasm. These data support that cell confinement leads to enhanced cPLA$_2$ activity and production of arachidonic acid associated with INM unfolding and stretching of the nucleus surface.

AA has been implicated to regulate myosin II activity both directly (*41*) and indirectly via protein phosphorylation (*42*). We tested the involvement of Rho/Rho associated protein kinase (ROCK) and Calcium/Myosin light chain kinase (MLCK) signaling that act as key regulatory pathways of myosin II activity (*4*). MLCK inhibition showed no significant effect on myosin II enrichment in confined cells, while a pronounced reduction of cortical myosin II recruitment was observed when using Staurosporin, a general kinase inhibitor, and under specific inhibition of Rho activity (Fig. 6F). Using a RhoA-Fret sensor further indicated an increased RhoA activity in confined cells versus control cells in suspension which was significantly reduced in the presence of cPLA$_2$ inhibitor in confined cells (Fig. S5F). These data support that AA production by cPLA$_2$ activity engages upon nuclear envelope unfolding, regulating phosphorylation-dependent myosin II activity at the cell cortex. AA and its metabolic products have been widely implicated in para- and autocrine signaling functions involving GPCRs (*43*). We assessed the role of AA product release by compressing cells directly under micropillars at an approximate height of 7 µm, leading to confined and non-confined cells in close proximity (Fig. S5G). Interestingly, while confined cells showed high levels of cortical myosin II and amoeboid cell transformation, non-confined cells in direct contact revealed no alterations in cortical myosin II and cellular morphodynamics (Fig. S5H). These results support that cPLA$_2$-dependent myosin II activation does not depend on the release of diffusible signals and regulates cellular morphodynamics via a cell autonomous increase of cortical contractility under cell deformation in confinement.

Interference with intracellular calcium levels by addition of BAPTA-AM or in combination with cPLA$_2$ inhibitor blocked myosin II enrichment in confined cells, without altering cortical myosin II levels in unconfined control cells (Fig. S5I). LPA stimulation of BAPTA-AM treated cells confirmed that myosin II can be activated by the Rho-ROCK signaling pathway in the absence of intracellular calcium and remains competent to bind the cell cortex (Fig. S5C). Similarly, chelating extracellular calcium reduced cortical myosin II re-localization, while depletion of internal calcium stores using Thapsigargin led to a slight increase in myosin II enrichment in confinement (Fig. S5I). The addition of ionomycin showed that high intracellular calcium levels, in the absence of cellular shape deformation, were not sufficient to evoke AA production (Fig. S5J) and cortical myosin II enrichment (Fig. S5B,D). This suggests that intracellular calcium has a permissive function for cPLA$_2$ association with the INM and increasing cortical contractility under cell

confinement. Our findings are in line with the observation that cPLA$_2$ contains a calcium-dependent C2 domain that modulates protein binding to the INM (*44-46*), which has been shown to get further enhanced and stabilized by mechanical stretching of the nucleus (*39*). Consistently, cPLA$_2$ showed a transient localization to the INM in the presence of ionomycin, while additional mechanical stretch due to hypotonic swelling or cell confinement induced a stable association with the INM (Fig. S3J-K).

INM unfolding and nucleus positioning enable to decode different types of cell shape deformations

To study if INM unfolding under cell confinement was sufficient to trigger cPLA$_2$ activity, we measured cortical myosin II levels and amoeboid migration competence under hypotonic swelling of cells. Quantification of nuclear shape parameters (size, volume, surface) revealed that hypotonic swelling induced comparable nuclear surface expansion and INM unfolding as nucleus deformation under a confinement height of 7 µm (Fig. S6A-C). Interestingly, cortical myosin II levels in hypotonic conditions (Fig. 7A, Movie 7) and associated changes in bleb size (Fig. S6D) and cell polarization rate (Fig. 7C) were significantly lower compared to cells deformed at 7 µm confinement height. These observations suggest that nuclear envelope unfolding alone is not sufficient to trigger high levels of cortical myosin II enrichment under isotropic cell stretching in hypotonic conditions versus anisotropic cell deformation in confinement.

Comparing intracellular calcium levels between deformed cells in confinement and under hypotonic conditions showed a pronounced increase in intracellular calcium concentrations in confined cells, with a specific calcium increase in the cell nucleus (Fig. 7B and Fig. S6E). This observation suggests that the level of intracellular calcium can modulate morphodynamic cellular responses to different mechanical shape deformations. Of note, ectopically increasing intracellular calcium levels under hypotonic conditions via the addition of ionomycin led to a pronounced and rapid increase in cortical myosin II enrichment in a cPLA$_2$-dependent manner (Fig. S6F, Movie 7) that triggered spontaneous cell polarization (Fig. 7C,D and S6G). Similar to cells in confinement, cell polarization under this condition was associated with a rapid transformation of non-motile cells into a highly motile stable-bleb amoeboid mode with fast migration speed under confinement ex vivo and in vivo (Fig. 7E and S6H,I,M, Movie 7,8). Raman spectroscopy to directly measure cPLA$_2$ activity confirmed that hypotonic stress increased AA levels (Fig. S5K) in a cPLA$_2$-dependent manner (S5L), with addition of ionomycin in hypotonic conditions further increasing AA production (S5M). Relative measured AA levels further directly correlated with cortical myosin II levels (Fig. S5N). Together, these data reveal that intracellular calcium levels are differentially regulated under distinct shape deformations and modulate cPLA$_2$ activity under similar INM stretch: uniaxial compression in confinement induces high intracellular calcium levels specifically in the nucleus, while isotropic radial stretch in hypotonic stress conditions leads to a lower intracellular calcium levels. Independently modulating nucleus deformation and calcium levels under different shape deformations confirmed that both parameters engage synergistically to regulate cortical contractility (Fig. 8A) and cellular dynamics under mechanical stress (Fig. 7E), thereby enabling a cell to distinguish between different types of shape deformation and to acquire a specific morphodynamic response.

Intracellular nucleus positioning appeared a promising candidate to differentially modulate calcium levels. ER-plasma membrane (ER-PM) proximity has been implicated as an important

regulator of cellular calcium signaling (*47*). Visualization of membrane proximal ER structures showed that the ER was highly dynamic under conditions of low confinement but was increasingly immobilized between the nucleus-PM interface for larger cell deformations in confinement (Movie 9). In addition, the expanding nucleus contact area close to the plasma membrane closely correlated with an intracellular calcium increase (Fig. S6J). We speculated that STIM-Orai, with STIM proteins located at the endoplasmic reticulum (ER) and Orai proteins representing calcium-selective plasma membrane (PM) calcium channels, could be involved in cellular calcium regulation in confined cells. STIM-Orai proteins have an established function in store operated calcium entry (SOCE) upon depletion of calcium from the ER which are mediated via ER-PM proximity (*48, 49*). Analysis of STIM-Orai protein localization revealed that both proteins accumulate at the interface between the nucleus and plasma membrane in confined cells at 7 µm (Fig. S6K,L). In contrast, we observed a homogenous distribution of both channels in cells under 13 µm confinement height when the ER was not spatially confined between the nucleus and PM. These data support that ER immobilization is associated with the specific enrichment of STIM-Orai in the ER-PM contact region where mechanical ER confinement occurs. Inhibition of the STIM-Orai complex by using 2APB further blocked myosin II enrichment under cell deformation in confinement (Fig. S5I). Our observations support that mechanical compression of the cell nucleus induces a tight connectivity between ER-PM structures and STIM-Orai localization at the ER-PM contact interface involved in the upregulation of intracellular calcium levels in confined cells.

Conclusions

Our data support that the nucleus establishes a core element to measure cellular shape deformation via two key physical parameters: 1) nuclear shape deformation leading to INM unfolding and 2) intracellular spatial positioning of the nucleus. In this model, INM unfolding under nuclear shape change allows for the deformation-dependent activation of $cPLA_2$ signaling, whereby $cPLA_2$ activity is modulated by intracellular calcium levels set by nucleus-PM proximity (Fig. 8B and S7A). The parameter space of these two variables (INM unfolding and calcium levels) provides a unique identifier for a cell to decode distinct shape deformations as exemplified on anisotropic cell deformation in confinement versus isotropic hypotonic cell stretching, allowing cells to acquire a unique adaptive response depending on the type of physical shape deformation (Fig. S7B).

Biochemical, physical and mechanical cues in the surrounding of a cell create manifold information for cells which is continuously sensed, integrated and transduced to allow for complex cellular functioning. Here we show that the cell nucleus functions as a cellular mechano-gauge for precisely decoding cellular shape changes, allowing cells to adaptively and rapidly tune cytoskeletal network properties and morphodynamic behavior within their 3D tissue microenvironment during development. This mechanism lays a foundation for functional principles underlying cellular proprioception that, comparable to the sensing of spatio-temporal changes in body posture and movement (*50*), enable a precise interpretation of shape changes on the single cell level.

The nucleus, being the largest organelle within the cell, represents a prominent structure to transmit and modulate mechanosensitive processes (*51-55*), and nucleus deformation has been shown to influence nuclear transport and cell differentiation (*56-58*), chromatin (*59-61*), migration (*62-66*) and pathfinding in constrained environments (*67*). Our findings support that nucleus deformation

and its intracellular positioning establish a cellular sensing module that equips cells to rapidly and reversibly adapt their dynamic response to shape fluctuations. This "nuclear ruler pathway" was also identified in an accompanying study (*68*), supporting its conservation between embryonic and differentiated cells in the adult organism. The observation of a rapid contractile cell response upon cell squeezing in confinement which is followed by fast amoeboid motility is reminiscent of a "cellular escape reflex" that enables cells to cope with physical constraints and acute deformations of their shape. Such a mechanism might be relevant for various biological processes associated with migration plasticity of cancer and immune cells in constrained 3D tissue niches (*69-72*) mechano-chemical feedback processes during morphogenesis (*73*) and homeostatic tissue functions such as cell density regulation (*74*), which require accurate mechanisms to detect variations in cellular size and shape and multicellular packing density in crowded 3D tissues.

Acknowledgments: The authors would like to acknowledge the Super Resolution Light Microcopy and Nanoscopy (SLN) Facility of ICFO for their support with imaging experiments and Johann Osmond (Nanofabrication laboratory, ICFO) for the design and production of molds for generating confinement coverslip, and further support from the CRG Core Facilities for Genomics and Advanced Light Microscopy. We thank the following labs that kindly provided plasmids: pCS2+ lefty/casanova (courtesy Carl-Philipp Heisenberg); pCS2+ lyn-TdTomato (courtesy Berta Alsina); pTriEx-RhoA FLARE.sc Biosensor WT was a gift from Klaus Hahn (Addgene plasmid #12150; RRID:Addgene_12150). We would like to thank Carl-Philipp Heisenberg, Matthieu Piel and Alexis J. Lomakin for discussions on this work and Ben Lehner, Vivek Malhotra, Sebastian P. Maurer and the Ruprecht and Wieser lab members for critical reading of the manuscript. **Funding:** V.V. acknowledges support from the ICFOstepstone - PhD Programme funded by the European Union's Horizon 2020 research and innovation programme under the Marie Skłodowska-Curie grant agreement No 665884. F.P. and Q.T. acknowledge a grant funded by "The Ministerio de Ciencia, Innovación y Universidades and Fondo Social Europeo (FSE)" (BES2017-080523-SO, PRE2018-084393). M.A.V. acknowledges support from the Spanish Ministry of Science, Education and Universities through grants RTI2018-099718-B-100 and an institutional "Maria de Maeztu" Programme for Units of Excellence in R&D and FEDER funds. J.W. was suppported by the Christian Doppler Forschungsgesellschaft (Josef Ressel Center for Phytogenic Drug Research). S.W. and M.K. acknowledge support from the Spanish Ministry of Economy and Competitiveness through the "Severo Ochoa" program for Centres of Excellence in R&D (SEV-2015-0522), from Fundació Privada Cellex, Fundación Mig-Puig and from Generalitat de Catalunya through the CERCA program and LaserLab (No 654148). M.K. acknowledges support through Spanish Ministry of Economy and Competitiveness (RYC-2015-17935, EQC2018-005048-P, AEI-010500-2018-228, PGC2018-097882-A-I00), Generalitat de Catalunya (2017 SGR 1012), the ERC (715243) and the HFSPO (CDA00023/2018). S.W. acknowledges support through the Spanish Ministry of Economy and Competitiveness via MINECO's Plan Nacional (BFU2017-86296-P). V.R. acknowledges support from the Spanish Ministry of Economy and Competitiveness through the Program "Centro de Excelencia Severo Ochoa 2013-2017", the CERCA Programme / Generalitat de Catalunya, MINECO's Plan Nacional (BFU2017-86296-P). **Author contributions:** V.R. and S.W. designed research; V.V. performed key experiments and data analysis; F.P. contributed to hypotonic and interference experiments and RNA preparations; F.C-C. and V.V. performed optical tweezers experiments and F.C. analyzed the data; M.M. and V.V. performed Raman experiments and M.M. analyzed the data; M.C-R. analyzed the Lap2B-GFP data; H-M.M. and Q.T.-R. performed in vivo experiments and H.-M.H.

performed injections and helped with mesendoderm-ectoderm experiments; S.J-D. cloned plasmids, synthetized mRNA and performed mRNA and bead injections; S.P-L. performed calcium imaging related to the role of Piezo channels; M.A.V. supervised S.P-L. and contributed with discussions and support to calcium imaging experiments; J.W. provided biological reagents and supported molecular cloning. M.K. supervised F.C.-C. and designed tweezer experiments. S.W. and V.R. supervised the project, contributed to data analysis and wrote the manuscript. **Competing interests:** The authors declare no competing financial interests. **Data and materials availability:** All data relevant for the conclusions of this work are available in the main text or the supplementary materials.

Supplementary Materials:

Supplementary Methods

Figures S1-S7

Supplementary Table S1

Supplementary Movies S1-S9

Supplementary References (*80-86*)

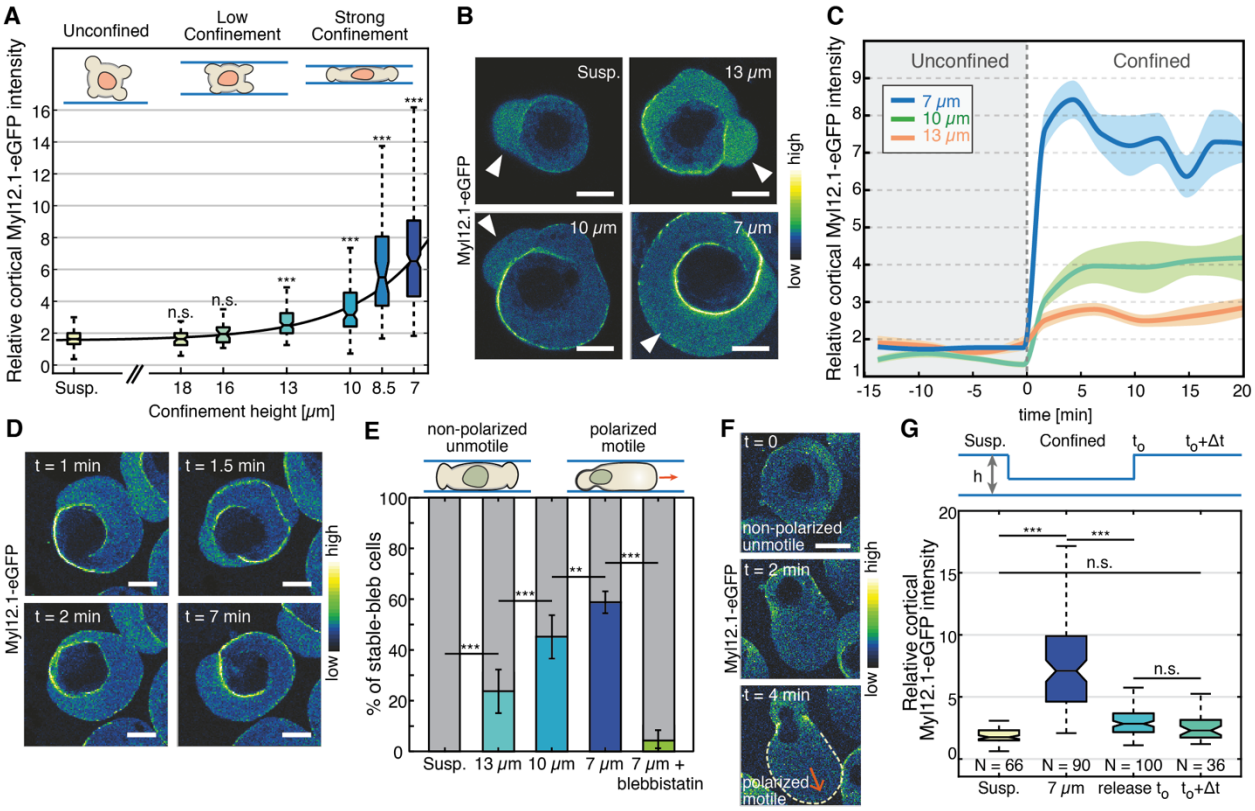

Figure 1. Cell deformation in confined environments defines cell contractility, polarization and fast amoeboid cell migration. (A) Relative cortical myosin II enrichment for decreasing confinement height in un-polarized progenitor cells (N=477 (suspension, unconfined); N=56 (18 μm); N=35 (16 μm); N=103 (13 μm); N=131 (10 μm); N=49 (8.5 μm); N=348 (7 μm)). Significance values are with respect to the suspension condition. Black line shows a mono-exponential fit with offset to the data. **(B)** Exemplary confocal fluorescence images of control progenitor stem cells in suspension (Susp.) and indicated confinement heights expressing Myl12.1-eGFP (myosin II). White arrows point at cellular blebs. **(C)** Temporal dynamics of cortical myosin II recruitment upon mechanical confinement at time t=0 at indicated heights. Thick lines correspond to the mean and areas to the standard error of the mean (sem). N>50 cells for all conditions. **(D)** Exemplary cross-sectional time-lapse images of myosin II-eGFP expressing cells under 7 μm confinement. **(E)** Percentage of polarized motile stable-bleb cells in suspension at

indicated confinement heights and myosin II inhibition (blebbistatin) at 7 µm (each N>500). **(F)** Representative time-lapse images of a myosin II-eGFP expressing cell undergoing spontaneous stable-bleb cell polarization and migration initiation. Dashed line shows the stable-bleb cell front and red arrow points in the direction of movement. **(G)** Relative cortical myosin II enrichment during reversible cell confinement. Cells were confined for 15 min before confinement was released and cortical myosin II levels were measured at t_0 (0-5 min) and at $t_0+\Delta t$ (30-60 min) after release. ***p<0.0001, **p<0.001, *p<0.01, not significant (n.s.). All scale bars 10 µm.

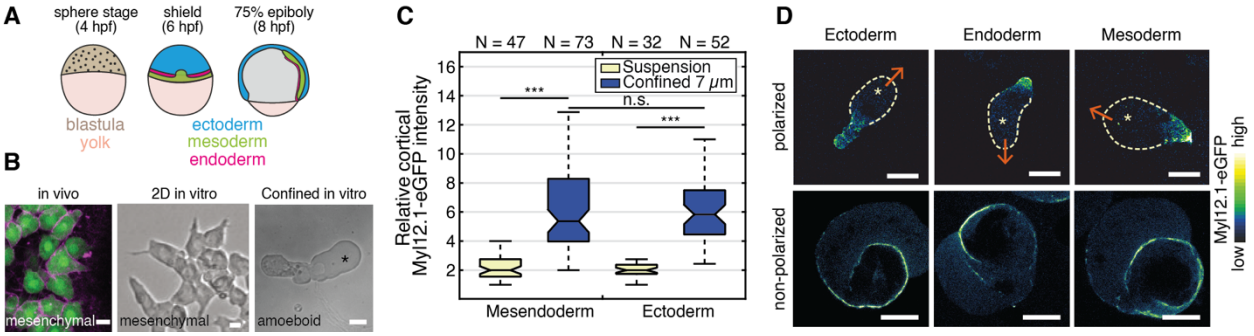

Figure 2. Physical confinement triggers amoeboid migration in different cell lineages. (A) Sketch of the developing zebrafish embryo at sphere (4 hpf), shield (6 hpf) and 75% epiboly (8 hpf) stage. **(B)** Exemplary confocal and bright field images of mesodermal cells in vivo expressing Lyn-Tomato (magenta, membrane) and GFP (green) under the mezzo promoter (left), induced mesendodermal cells in vitro plated on a 2D fibronectin-coated surface (middle) and under 7 µm confinement (right), asterisk points at stable-bleb cell front. **(C)** Relative cortical myosin II intensity for mesendodermal and ectodermal progenitor cells in control suspension and confinement conditions. **(D)** Exemplary confocal images of stable-bleb polarized (top) and non-polarized (bottom) progenitor cell types expressing myosin II-eGFP under 7 µm confinement. From left to right: ectoderm, endoderm and mesoderm cells. Dashed line and yellow asterisks indicate the stable-bleb cell front and red arrows the direction of cell migration. ***p<0.0001, **p<0.001, *p<0.01, not significant (n.s.). All scale bars 10 µm.

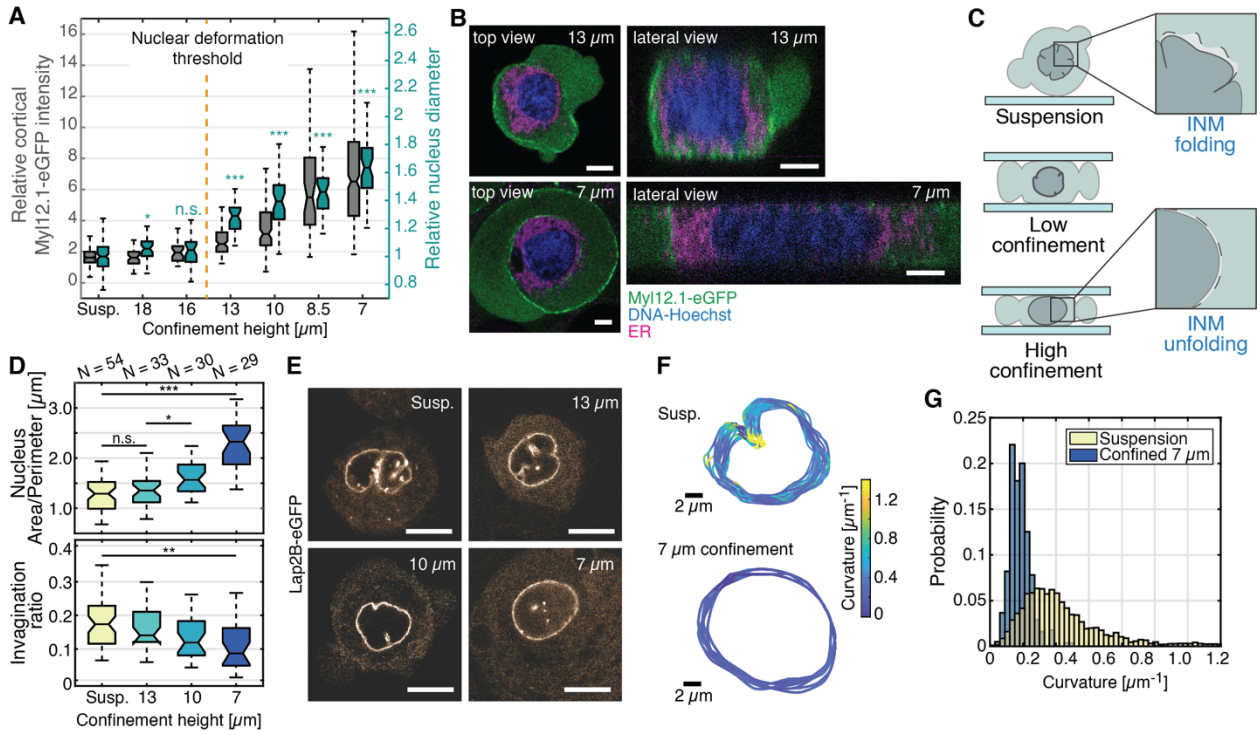

Figure 3. Nuclear envelop unfolding is associated with increasing cortical contractility. (A) Double boxplot of relative cortical myosin II enrichment (left axis, grey) and relative nuclear diameter (right axis, green) for decreasing confinement height. Statistical test for relative nuclear diameter performed with respect to suspension (N=144 (suspension); N=44 (18 µm); N=32 (16 µm); N=37 (13 µm); N=45 (10 µm); N=37 (8.5 µm); N=50 (7 µm)). Statistical tests for cortical myosin II levels and experimental N related to Fig.1A. **(B)** Exemplary confocal top views (x-y) and lateral views (y-z) of progenitor stem cells expressing myosin II-eGFP stained with DNA-Hoechst and ER-TrackerRed in 13 µm and 7 µm confinement. **(C)** Illustration showing the unfolding of the inner nuclear membrane (INM) with increasing cell confinement. **(D)** Nuclear area to perimeter ratio (top) and nuclear invagination ratio (bottom) for increasing confinement. **(E)** Exemplary confocal images of cells expressing Lap2B-eGFP under varying cell deformation. **(F)** Curvature analysis of nuclear shape for 20 consecutive frames (t_{lag}=10 s) for unconfined (suspension, top) and 7 µm confined nuclei (bottom). **(G)** Histogram of nuclear curvature for

unconfined and 7 µm confined nuclei related to panel F with N=10 cells for each condition ($p<10^{-12}$, ***). ***$p<0.0001$, **$p<0.001$, * $p<0.01$, not significant (n.s.). All scale bars 10 µm despite 5 µm in (B).

5

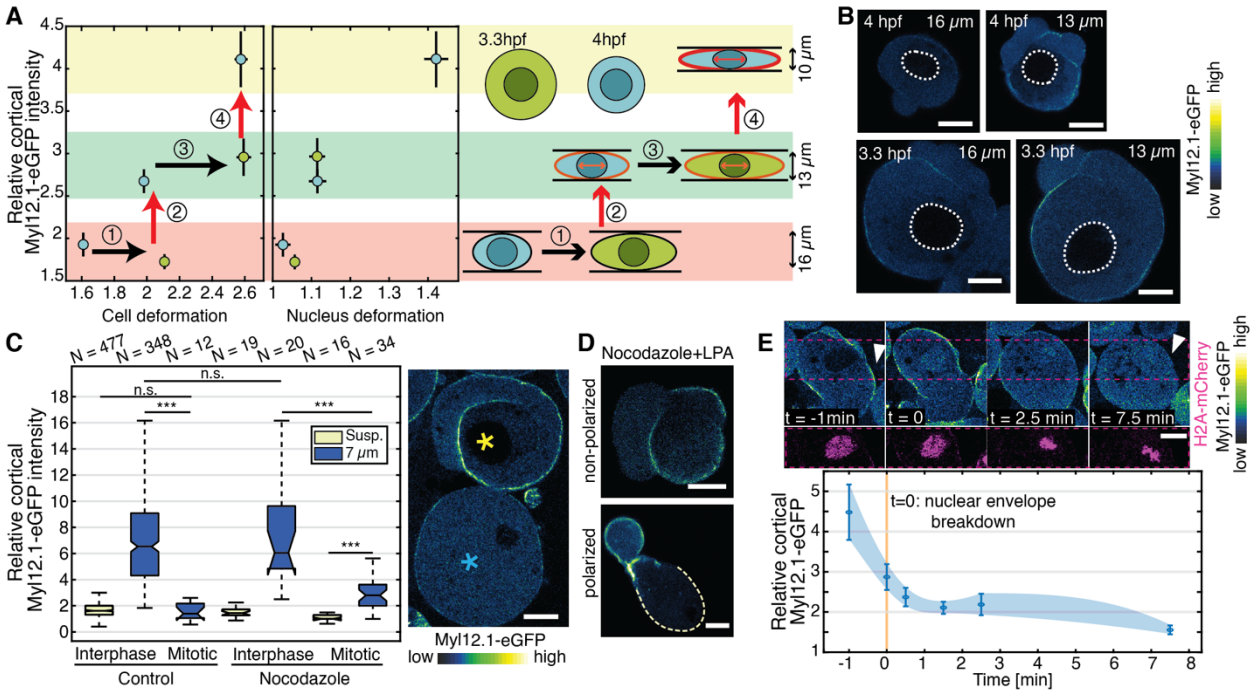

Figure 4. Nucleus size and integrity determine the morphodynamic cell response to confinement. (A) Relative cortical myosin II intensity with respect to cell deformation as defined by the ratio of cell size/confinement height (left) and nucleus deformation (right) measured via relative nucleus diameter increase (right) for cells dissociated from embryos at high-oblong (3.3 hpf) and sphere stage (4 hpf) and cultured under similar confinement heights as indicated. Data points and error bars indicate mean and standard error of the mean (sem); (3.3 hpf: 16 µm N=58, 13 µm N=61; 4 hpf: 16 µm N=44, 13 µm N=60, 10 µm N=45). The Pearson correlation coefficient in between myosin II intensity and nuclear deformation is 0.48. **(B)** Exemplary confocal images of progenitor cells expressing myosin II-eGFP under 16/13 µm confinement dissociated from 4 hpf (top) and 3.3 hpf (bottom) embryos. Dashed lines outline cell nuclei. **(C)** Relative cortical myosin II enrichment for interphase and mitotic cells under 7 µm confinement cultured in suspension (control) in the presence of 1 µM Nocodazole. Exemplary confocal images of progenitor cells expressing myosin-II-eGFP in interphase (yellow asterisk) or during mitosis (cyan

asterisk) under 7 µm confinement. **(D)** Exemplary confocal images of progenitor unpolarized (top) and polarized (bottom) cells expressing myosin-II-eGFP during mitosis treated with 1 µM Nocodazole and 50 µM LPA. Dashed line shows the stable-bleb cell front. (**E**) Cortical myosin II intensity of N=7 cells undergoing mitosis and representative confocal time lapse images of cells expressing myosin-II-eGFP and H2A-mCherry at indicated time points (t=0: time of nuclear envelope breakdown). The arrows point at the cell cortex with cortical myosin enrichment (t=-1min) or loss of cortical myosin levels (t=7.5min). Data points and error bars indicate mean and standard error of the mean. ***p<0.0001, **p<0.001, * p<0.01, not significant (n.s.). All scale bars 10 µm.

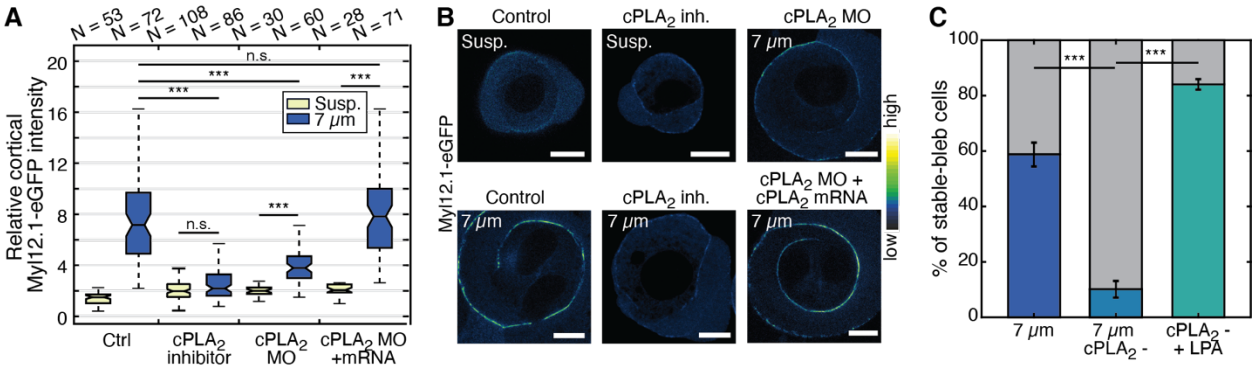

Figure 5. Nucleus deformation activates a mechanosensitive lipase signaling pathway regulating myosin II activity. (A) Relative cortical myosin II intensity for progenitor cells cultured in suspension versus 7 µm confinement conditions for control cells (DMEM), with cPLA$_2$ inhibitor, or injected with cPLA$_2$ MO and cPLA$_2$ MO + cPLA$_2$ mRNA. **(B)** Exemplary confocal images of progenitor cells expressing myosin II-eGFP related to (A) for indicated conditions. **(C)** Percentage of stable-bleb polarized cells for control cells under 7 µm confinement and in the presence of cPLA$_2$ inhibitor or unconfined (suspension) cells stimulated with 50 µM LPA. For all conditions N>200. ***p<0.0001, **p<0.001, *p<0.01, not significant (n.s.). All scale bars 10 µm.

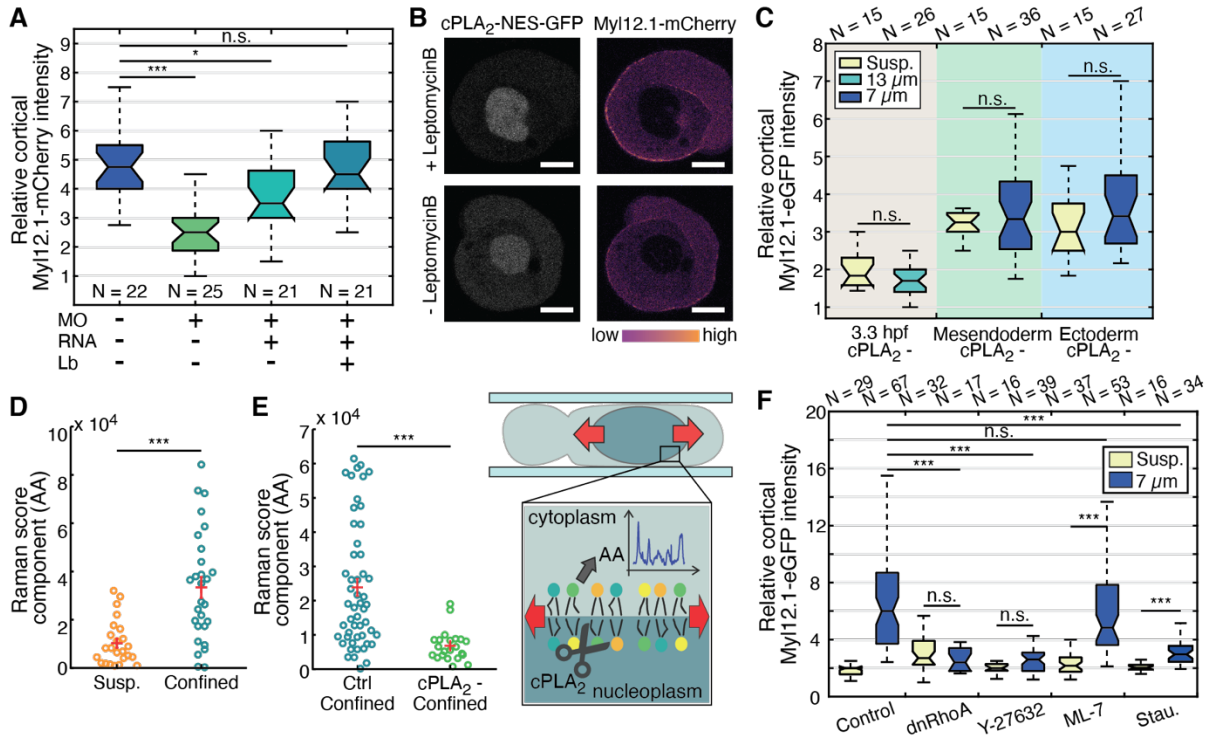

Figure 6. cPLA2 activity at the inner nuclear membrane generates AA as a metabolite regulating cortical contractility in confinement. (A) Relative cortical myosin II fluorescence intensity for cells dissociated from controls (un-injected) embryos or embryos injected with $cPLA_2$ MO, $cPLA_2$ MO + $cPLA_2$-NES-GFP mRNA (RNA) and with or without addition of Leptomycin B (Lb). **(B)** Exemplary confocal fluorescence images of cell expressing myosin II-mCherry (right) and $cPLA_2$-NES-GFP (left) under 7 µm confinement with (top) or without (bottom) the addition of Lb. **(C)** Relative cortical myosin II fluorescence intensity upon $cPLA_2$ inhibition for cells dissociated at 3.3 hpf, induced mesendoderm or ectoderm cells in suspension and upon confinement at indicated height. **(D, E)** Scores of Raman component associated to AA in suspension (unconfined, N=24) and confined cells (10 µm, N=28) and (H) in control confinement condition (Ctrl, N=52) or treated with $cPLA_2$ inhibitor (N=22). Red lines indicate mean and sem. **(F)** Relative cortical myosin II intensity for control cells and different chemical (Y-27637, M-L7,

Staurosporine) or genetic interference (dnRhoA) with myosin II regulators. ***p<0.0001, **p<0.001, *p<0.01, not significant (n.s.). All scale bars 10 μm.

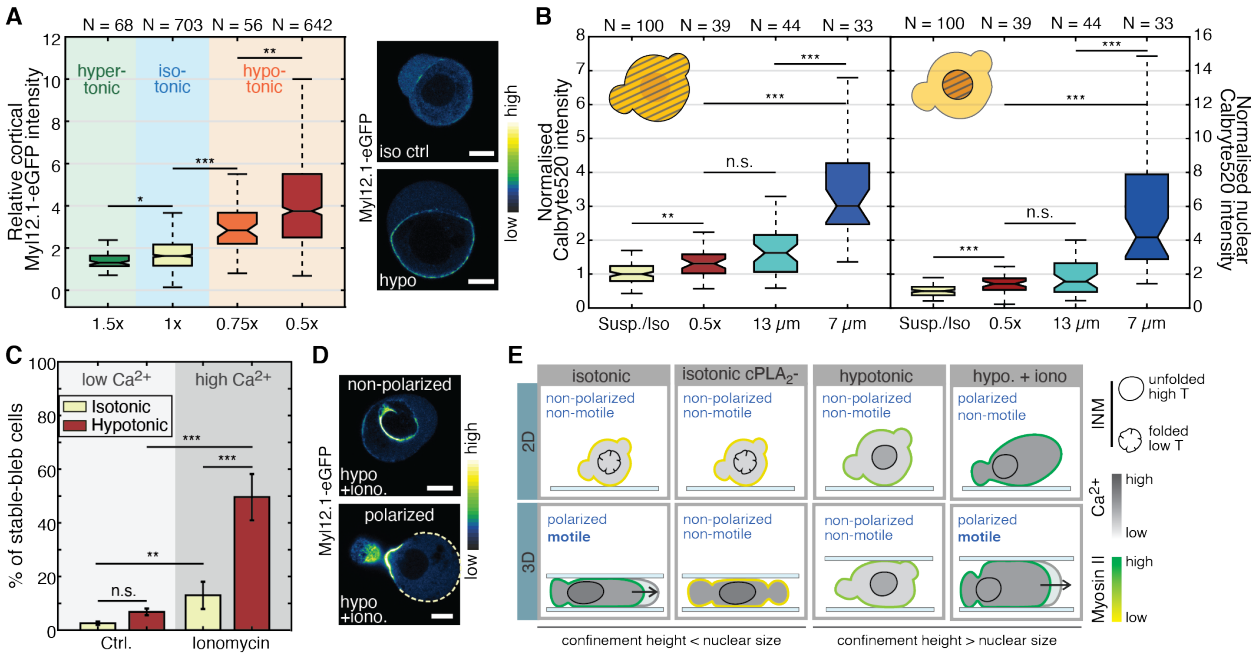

Figure 7. Nucleus stretch and intracellular positioning enable an adaptive cellular response to different types of physical cell deformation. (A) Relative cortical myosin II enrichment for progenitor cells cultured under different osmolarity conditions. **(B)** Normalized cell (left) and nuclear (right) Ca^{2+} levels (Calbryte520) for control (Ctrl) and hypotonic (0.5 x) conditions and mechanical confinement (13 µm, 7 µm). **(C)** Percentage of stable-bleb polarized cells in isotonic and hypotonic (0.5 x) conditions for cells cultured in DMEM (Ctrl) or supplemented with 1 µM ionomycin. N>1000 cells for all conditions. **(D)** Exemplary confocal images of cells expressing myosin II-eGFP in isotonic (ctrl, top-left), hypotonic (bottom-left) and hypotonic conditions supplemented with ionomycin treatment (right): non-polarized cell (top) and stable-bleb polarized cell (bottom). **(E)** Sketch of cell polarization and motile cell behavior in 2D (top) versus 3D confined environments (bottom) and for control conditions (isotonic media; first column) versus $cPLA_2$ interference (second column) and hypotonic condition alone (third column) or in the presence of ionomycin (fourth column). ***p<0.0001, **p<0.001, *p<0.01, not significant (n.s.). Scale bars 10 µm.

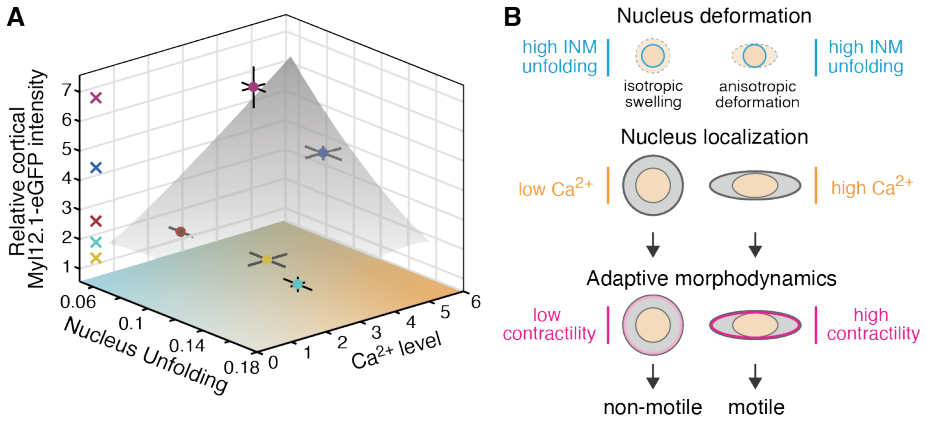

Figure 8. INM unfolding and intracellular calcium levels enable cells to decode isotropic stretch versus cell squeezing in confinement. (**A**) Normalized relative cortical myosin II fluorescence intensity as a function of nucleus unfolding and normalized Ca^{2+} (Calbryte) intensity for different physical cell deformations (dark blue: 7 µm; light blue: 13 µm confinement; yellow: 7 µm confinement + Bapta-AM; red: hypotonic (0.5x) condition; magenta: hypotonic condition (0.5x) + ionomycin). Data indicate mean and sem. The gray area sketches the relation between cortical myosin II and nuclear deformation versus intracellular calcium levels. (N: calcium data related to Fig. 4B, except for hypo + ionomycin (N=41) and Bapta-AM + 7 µm N=9; for nuclear unfolding related to Fig. 2D, Fig S6B and for cortical myosin II levels to Fig. 1A, S5I, 4A, S6F). (**B**) Sketch depicting how nucleus deformation and intracellular nucleus positioning correlate with INM unfolding and intracellular calcium levels, which differentially regulate cortical contractility and cellular morphodynamics. ***p<0.0001, **p<0.001, *p<0.01, not significant (n.s.). Scale bars 10 µm.

Materials and Methods

Zebrafish Maintenance Zebrafish (Danio rerio) were maintained as previously described (*75*). Embryos were kept in E3 medium at 25°C–31°C prior to experiments and staged based on morphological criteria (*76*) and hours post fertilization (hpf). Wild type embryos were obtained from the AB strain background. All protocols used have been approved by the Institutional Animal Care and Use Ethic Committee (PRBB–IACUEC) and implemented according to national and European regulations. All experiments were carried out in accordance with the principles of the 3Rs.

Transgenic fish lines The following transgenic lines were used: Tg(actb2:Lifeact-GFP) (*77*), Tg(actb2:Myl12.1-eGFP) (*78*), Tg(actb2:Myl12.1-mcherry) (*4*), Tg(mezzo:eGFP) (*23*), Tg(actb2:Lyn-TdTomato) (*79*). All progenitor cells expressing Myl12.1-eGFP (Myosin II) and Lifeact-GFP (Actin) were obtained from Tg(actb2:Myl12.1-eGFP) and Tg(actb2:Lifeact-GFP).

Cell culture To culture progenitor cells, embryos were manually dechorionated in E3 buffer at sphere stage (4 hpf) or different stages if indicated. Five to twenty embryos were transferred to DMEM-F12 (with L-Glut and 15mM HEPES, without sodium bicarbonate and phenol red) culture medium (Sigma) and mechanically dissociated by manual tapping followed by centrifugation at 200 g for 3 min.

Sample preparation and surface coatings The following products for surface coatings at the indicated concentration have been used: 0.5 mg/ml PLL(20)-g[3,5]-PEG(2) (Susos) and 0.2 mg/ml fibronectin (Sigma-Aldrich). Prior to PLL-PEG coating, both coverslips and dishes were plasma cleaned. Uncoated or PLL-coated glass dishes #1.5 were purchased from MatTek (MatTek Corporation).

Cell confiner Cells were confined using a dynamic confiner (4DCell) similar to previously established planar microconfinement methods (*30*). In order to confine cells at different heights, multiple Si molds were produced by photolithography in a clean room (Nanofabrication laboratory, ICFO) by depositing a SU-8 resin on a silicon wafer. In brief, a photomask with the desired geometry was created. Confinement coverslips were prepared with polydimethylsiloxane (PDMS) with the following heights: 18, 16, 13, 10, 8.5 and 7 µm. Coverslips were always plasma cleaned, coated with PLL-PEG if not indicated otherwise and equilibrated in DMEM prior to each experiment. A pressure pump (AF1 – Microfluidic pressure pump, Elveflow) together with the ESI software was used to change the pressure for tuning the confinement heights. For Raman measurements and optical tweezers two coverslips separated with microbeads or with a PDMS membrane have been used (height h=10 µm).

Reagents and inhibitor treatments Pharmacological inhibitors were used at the following concentrations: 1 µM $cPLA_2$ inhibitor (Pyrrophenone, Merck-Millipore), 10 µM Bapta-AM (Cayman), 10 µM Blebbistatin (+) (Tocris Bioscience), 10 µM Y-27632 (Tocris Bioscience), 10 µM ML-7 hydrochloride (Tocris Bioscience), 1 µM Nocodazole (Sigma), 50 nM LeptomycinB (Sigma-Aldrich), 1 µM Ionomycin (Sigma-Aldrich), 1 µM Thapsigargin (Thermofisher), 10 µM GsMTx4 (Tocris), 50 µM 2-APB (Biogen-Santa Cruz), 10 µM Gadolinium chloride (Tocris), 2 µM Actinomycin D (PanReac), 100 µM Z-VAD(OMe)-FMK (Abcam), 1 µM Staurosporine (Abcam), 1-oleoyl lysophosphatidic acid (LPA, Tocris Bioscience) was used at the indicated concentrations. Measurements were done directly after exposure to MLCK inhibitor, GsMTx4, Ionomycin, LPA; all the other inhibitors have been pre-incubated for 30 min and 60 min for Y-27632 prior to experiments.

Fluorescence staining Calbryte520 (AAT BIOQUEST) was used to study calcium dynamics. The staining kit-Red Fluorescence-Cytopainter (ER Tracker, Abcam) or ER-Tracker™ Green (BODIPY™ FL Glibenclamide) were used to visualize the endoplasmic reticulum respectively for confocal 3D colors imaging and for TIRF microscopy experiment. DNA-Hoechst (Thermofisher) was used to stain the cell nucleus. Cells were incubated with Calbryte520 for 20 min, with ER-tracker for 30 min and with DNA-Hoechst for 7-10 min as reported in the corresponding protocols and at the indicated concentrations. After incubation, cells were washed, centrifuged at 200 g for 3 min and re-suspended in DMEM media.

Variable osmotic culture conditions D-Mannitol (Sigma) was diluted in DMEM in order to obtain a culture medium with an osmolarity of approx. 450 mOsm/l (corresponding to a 1.5x media). Milli-Q water was added to DMEM for hypotonic conditions.

References

1. G. Salbreux, G. Charras, E. Paluch, Actin cortex mechanics and cellular morphogenesis. *Trends Cell Biol* 22, 536-545 (2012).
2. N. W. Goehring, S. W. Grill, Cell polarity: mechanochemical patterning. *Trends Cell Biol* 23, 72-80 (2013).
3. A. C. Callan-Jones, R. Voituriez, Actin flows in cell migration: from locomotion and polarity to trajectories. *Curr Opin Cell Biol* 38, 12-17 (2016).
4. M. Vicente-Manzanares, X. Ma, R. S. Adelstein, A. R. Horwitz, Non-muscle myosin II takes centre stage in cell adhesion and migration. *Nat Rev Mol Cell Biol* 10, 778-790 (2009).
5. M. A. Wozniak, C. S. Chen, Mechanotransduction in development: a growing role for contractility. *Nat Rev Mol Cell Biol* 10, 34-43 (2009).
6. T. Lecuit, P. F. Lenne, E. Munro, Force generation, transmission, and integration during cell and tissue morphogenesis. *Annu Rev Cell Dev Biol* 27, 157-184 (2011).
7. E. M. Balzer *et al.*, Physical confinement alters tumor cell adhesion and migration phenotypes. *FASEB J* 26, 4045-4056 (2012).
8. K. J. Sonnemann, W. M. Bement, Wound repair: toward understanding and integration of single-cell and multicellular wound responses. *Annu Rev Cell Dev Biol* 27, 237-263 (2011).
9. J. Briscoe, S. Small, Morphogen rules: design principles of gradient-mediated embryo patterning. *Development* 142, 3996-4009 (2015).
10. G. Charras, E. Sahai, Physical influences of the extracellular environment on cell migration. *Nat Rev Mol Cell Biol* 15, 813-824 (2014).
11. P. Roca-Cusachs, R. Sunyer, X. Trepat, Mechanical guidance of cell migration: lessons from chemotaxis. *Curr Opin Cell Biol* 25, 543-549 (2013).
12. M. Duda *et al.*, Polarization of Myosin II Refines Tissue Material Properties to Buffer Mechanical Stress. *Developmental Cell* 48, 245-260.e247 (2019).
13. A. Sumi *et al.*, Adherens Junction Length during Tissue Contraction Is Controlled by the Mechanosensitive Activity of Actomyosin and Junctional Recycling. *Dev Cell* 47, 453-463 e453 (2018).
14. J. Aureille *et al.*, Nuclear envelope deformation controls cell cycle progression in response to mechanical force. *EMBO Rep* 20, e48084 (2019).
15. S. A. Gudipaty *et al.*, Mechanical stretch triggers rapid epithelial cell division through Piezo1. *Nature* 543, 118-121 (2017).
16. E. Marinari *et al.*, Live-cell delamination counterbalances epithelial growth to limit tissue overcrowding. *Nature* 484, 542-545 (2012).
17. G. T. Eisenhoffer *et al.*, Crowding induces live cell extrusion to maintain homeostatic cell numbers in epithelia. *Nature* 484, 546-549 (2012).
18. M. Georgouli *et al.*, Regional Activation of Myosin II in Cancer Cells Drives Tumor Progression via a Secretory Cross-Talk with the Immune Microenvironment. *Cell*, (2019).
19. J. H. Kim *et al.*, Mechanical tension drives cell membrane fusion. *Dev Cell* 32, 561-573 (2015).
20. T. Luo, K. Mohan, P. A. Iglesias, D. N. Robinson, Molecular mechanisms of cellular mechanosensing. *Nat Mater* 12, 1064-1071 (2013).

21. C. J. Cattin *et al.*, Mechanical control of mitotic progression in single animal cells. *Proc Natl Acad Sci U S A* 112, 11258-11263 (2015).
22. T. Lämmermann, M. Sixt, Mechanical modes of 'amoeboid' cell migration. *Current opinion in cell biology* 21, 636-644 (2009).
23. V. Ruprecht *et al.*, Cortical contractility triggers a stochastic switch to fast amoeboid cell motility. *Cell* 160, 673-685 (2015).
24. J. S. Logue *et al.*, Erk regulation of actin capping and bundling by Eps8 promotes cortex tension and leader bleb-based migration. *Elife* 4, e08314 (2015).
25. A. W. Holle *et al.*, Cancer Cells Invade Confined Microchannels via a Self-Directed Mesenchymal-to-Amoeboid Transition. *Nano Lett* 19, 2280-2290 (2019).
26. T. Brunet, M. Albert, W. Roman, D. C. Spitzer, N. King, (2020).
27. M. Ibo, V. Srivastava, D. N. Robinson, Z. R. Gagnon, Cell Blebbing in Confined Microfluidic Environments. *PLoS One* 11, e0163866 (2016).
28. Y. J. Liu *et al.*, Confinement and low adhesion induce fast amoeboid migration of slow mesenchymal cells. *Cell* 160, 659-672 (2015).
29. R. Zhao *et al.*, Cell sensing and decision-making in confinement: The role of TRPM7 in a tug of war between hydraulic pressure and cross-sectional area. *Sci Adv* 5, eaaw7243 (2019).
30. M. Le Berre, E. Zlotek-Zlotkiewicz, D. Bonazzi, F. Lautenschlaeger, M. Piel, Methods for two-dimensional cell confinement. *Methods Cell Biol* 121, 213-229 (2014).
31. M. Bergert *et al.*, Force transmission during adhesion-independent migration. *Nat Cell Biol* 17, 524-529 (2015).
32. M. Krieg *et al.*, Tensile forces govern germ-layer organization in zebrafish. *Nat Cell Biol* 10, 429-436 (2008).
33. L. Solnica-Krezel, D. S. Sepich, Gastrulation: making and shaping germ layers. *Annu Rev Cell Dev Biol* 28, 687-717 (2012).
34. A. D. Bershadsky, N. Q. Balaban, B. Geiger, Adhesion-dependent cell mechanosensitivity. *Annu Rev Cell Dev Biol* 19, 677-695 (2003).
35. A. Saha *et al.*, Determining Physical Properties of the Cell Cortex. *Biophys J* 110, 1421-1429 (2016).
36. W. C. Hung *et al.*, Confinement Sensing and Signal Optimization via Piezo1/PKA and Myosin II Pathways. *Cell Rep* 15, 1430-1441 (2016).
37. N. I. Petridou, S. Grigolon, G. Salbreux, E. Hannezo, C. P. Heisenberg, Fluidization-mediated tissue spreading by mitotic cell rounding and non-canonical Wnt signalling. *Nat Cell Biol* 21, 169-178 (2019).
38. K. N. Dahl, S. M. Kahn, K. L. Wilson, D. E. Discher, The nuclear envelope lamina network has elasticity and a compressibility limit suggestive of a molecular shock absorber. *J Cell Sci* 117, 4779-4786 (2004).
39. B. Enyedi, M. Jelcic, P. Niethammer, The Cell Nucleus Serves as a Mechanotransducer of Tissue Damage-Induced Inflammation. *Cell* 165, 1160-1170 (2016).
40. E. A. Dennis, J. Cao, Y. H. Hsu, V. Magrioti, G. Kokotos, Phospholipase A2 enzymes: physical structure, biological function, disease implication, chemical inhibition, and therapeutic intervention. *Chem Rev* 111, 6130-6185 (2011).
41. T. Katayama *et al.*, Stimulatory effects of arachidonic acid on myosin ATPase activity and contraction of smooth muscle via myosin motor domain. *Am J Physiol Heart Circ Physiol* 298, H505-514 (2010).

42. M. Brown, J. A. Roulson, C. A. Hart, T. Tawadros, N. W. Clarke, Arachidonic acid induction of Rho-mediated transendothelial migration in prostate cancer. *Br J Cancer* 110, 2099-2108 (2014).
43. L. Sun, R. D. Ye, Role of G protein-coupled receptors in inflammation. *Acta Pharmacol Sin* 33, 342-350 (2012).
44. M. Peters-Golden, K. Song, T. Marshall, T. Brock, Translocation of cytosolic phospholipase A2 to the nuclear envelope elicits topographically localized phospholipid hydrolysis. *Biochem J* 318 (Pt 3), 797-803 (1996).
45. A. Dessen *et al.*, Crystal structure of human cytosolic phospholipase A2 reveals a novel topology and catalytic mechanism. *Cell* 97, 349-360 (1999).
46. J. E. Burke, E. A. Dennis, Phospholipase A2 biochemistry. *Cardiovasc Drugs Ther* 23, 49-59 (2009).
47. A. Gallo, C. Vannier, T. Galli, Endoplasmic Reticulum-Plasma Membrane Associations:Structures and Functions. *Annu Rev Cell Dev Biol* 32, 279-301 (2016).
48. S. Carrasco, T. Meyer, STIM proteins and the endoplasmic reticulum-plasma membrane junctions. *Annu Rev Biochem* 80, 973-1000 (2011).
49. X. Qin *et al.*, Increased Confinement and Polydispersity of STIM1 and Orai1 after Ca(2+) Store Depletion. *Biophys J* 118, 70-84 (2020).
50. R. Das, S. Wieser, M. Krieg, Neuronal stretch reception - Making sense of the mechanosense. *Exp Cell Res* 378, 104-112 (2019).
51. T. J. Kirby, J. Lammerding, Emerging views of the nucleus as a cellular mechanosensor. *Nat Cell Biol* 20, 373-381 (2018).
52. Z. Jahed, M. R. Mofrad, The nucleus feels the force, LINCed in or not! *Curr Opin Cell Biol* 58, 114-119 (2019).
53. C. S. Janota, F. J. Calero-Cuenca, E. R. Gomes, The role of the cell nucleus in mechanotransduction. *Curr Opin Cell Biol* 63, 204-211 (2020).
54. R. P. Martins, J. D. Finan, F. Guilak, D. A. Lee, Mechanical regulation of nuclear structure and function. *Annu Rev Biomed Eng* 14, 431-455 (2012).
55. Y. Xia, C. R. Pfeifer, S. Cho, D. E. Discher, J. Irianto, Nuclear mechanosensing. *Emerg Top Life Sci* 2, 713-725 (2018).
56. A. Elosegui-Artola *et al.*, Force Triggers YAP Nuclear Entry by Regulating Transport across Nuclear Pores. *Cell*, (2017).
57. J. Swift *et al.*, Nuclear Lamin-A Scales with Tissue Stiffness and Enhances Matrix-Directed Differentiation. *Science (New York, N.Y.)* 341, 1240104-1240104 (2013).
58. M. Almonacid, M. E. Terret, M. H. Verlhac, Nuclear positioning as an integrator of cell fate. *Curr Opin Cell Biol* 56, 122-129 (2019).
59. K. Damodaran *et al.*, Compressive force induces reversible chromatin condensation and cell geometry dependent transcriptional response. *Mol Biol Cell*, mbcE18040256 (2018).
60. A. Kumar *et al.*, ATR mediates a checkpoint at the nuclear envelope in response to mechanical stress. *Cell* 158, 633-646 (2014).
61. M. M. Nava *et al.*, Heterochromatin-Driven Nuclear Softening Protects the Genome against Mechanical Stress-Induced Damage. *Cell*, (2020).
62. A. L. McGregor, C.-R. Hsia, J. Lammerding, Squish and squeeze — the nucleus as a physical barrier during migration in confined environments. *Current Opinion in Cell Biology* 40, 32-40 (2016).

63. R. Majumdar, K. Steen, P. A. Coulombe, C. A. Parent, Non-canonical processes that shape the cell migration landscape. *Curr Opin Cell Biol* 57, 123-134 (2019).
64. R. J. Petrie, H. Koo, K. M. Yamada, Generation of compartmentalized pressure by a nuclear piston governs cell motility in a 3D matrix. *Science* 345, 1062-1065 (2014).
65. C. M. Denais *et al.*, Nuclear envelope rupture and repair during cancer cell migration. *Science* 352, 353-358 (2016).
66. M. Raab *et al.*, ESCRT III repairs nuclear envelope ruptures during cell migration to limit DNA damage and cell death. *Science* 352, 359-362 (2016).
67. J. Renkawitz *et al.*, Nuclear positioning facilitates amoeboid migration along the path of least resistance. *Nature* 568, 546-550 (2019).
68. A. J. Lomakin *et al.*, (2019).
69. S. van Helvert, C. Storm, P. Friedl, Mechanoreciprocity in cell migration. *Nat Cell Biol* 20, 8-20 (2018).
70. H. D. Moreau, M. Piel, R. Voituriez, A. M. Lennon-Dumenil, Integrating Physical and Molecular Insights on Immune Cell Migration. *Trends Immunol* 39, 632-643 (2018).
71. V. Te Boekhorst, L. Preziosi, P. Friedl, Plasticity of Cell Migration In Vivo and In Silico. *Annu Rev Cell Dev Biol* 32, 491-526 (2016).
72. D. Wirtz, K. Konstantopoulos, P. C. Searson, The physics of cancer: the role of physical interactions and mechanical forces in metastasis. *Nat Rev Cancer* 11, 512-522 (2011).
73. E. Hannezo, C.-P. Heisenberg, Mechanochemical Feedback Loops in Development and Disease. *Cell* 178, 12-25 (2019).
74. S. A. Gudipaty, J. Rosenblatt, Epithelial cell extrusion: Pathways and pathologies. *Semin Cell Dev Biol* 67, 132-140 (2017).
75. W. Westerfield, The zebrafish book: a guide for the laboratory use of zebrafish (Brachydanio rerio). (1995).
76. C. B. Kimmel, W. W. Ballard, S. R. Kimmel, B. Ullmann, T. F. Schilling, Stages of embryonic development of the zebrafish. *Dev Dyn* 203, 253-310 (1995).
77. M. Behrndt *et al.*, Forces driving epithelial spreading in zebrafish gastrulation. *Science* 338, 257-260 (2012).
78. J. L. Maitre *et al.*, Adhesion functions in cell sorting by mechanically coupling the cortices of adhering cells. *Science* 338, 253-256 (2012).
79. J. Compagnon *et al.*, The notochord breaks bilateral symmetry by controlling cell shapes in the zebrafish laterality organ. *Dev Cell* 31, 774-783 (2014).